KeAi
CHINESE ROOTS
GLOBAL IMPACT

Contents lists available at ScienceDirect

Petroleum Science

journal homepage: www.keaipublishing.com/en/journals/petroleum-science



Original Paper

A study on numerical simulation method of Cs2LiYCl6:Ce3+ detection response in neutron well logging



Qi-Xuan Liang ^{a,b}, Feng Zhang ^{a,b,*}, Jun-Ting Fan ^{a,b}, Dong-Ming Liu ^c, Yun-Bo Zhou ^c, Qing-Chuan Wang ^d, Di Zhang ^d

- ^a State Key Laboratory of Deep Oil and Gas, China University of Petroleum (East China), Qingdao, 266580, Shandong, China
- ^b School of Geosciences, China University of Petroleum (East China), Qingdao, 266580, Shandong, China
- ^cChangqing Branch, China Petroleum Logging Co., Ltd, Xi'an, 710201, Shaanxi, China
- d Exploration and Development Research Institute, PetroChina Qinhai Oilfield Company, Dunhuang, 736202, Gansu, China

ARTICLE INFO

Article history: Received 9 September 2024 Received in revised form 20 April 2025 Accepted 29 May 2025 Available online 3 June 2025

Edited by Meng-Jiao Zhou

Keywords:
Neutron well logging
Cs₂LiYCl₆:Ce³⁺ scintillator
Double-particle logging detection
Porosity determination
Monte Carlo simulation

ABSTRACT

Neutron well logging, using instruments equipped with neutron source and detectors (e.g., ³He-tubes, Nal, BGO), plays a key role in lithological differentiation, porosity determination, and fluid property evaluation in the petroleum industry. The growing trend of multifunctional neutron well logging, which enables simultaneous extraction of multiple reservoir characteristics, requiring high-performance detectors capable of withstanding high-temperature downhole conditions, limited space, and instrument vibrations, while also detecting multiple particle types. The Cs₂LiYCl₆:Ce³⁺ (CLYC) elpasolite scintillator demonstrates excellent temperature resistance and detection efficiency, making it become a promising candidate for leading the development of the novel neutron-based double-particle logging technology. This study employed Monte Carlo simulations to generate equivalent gamma spectra and proposed a pulse shape discrimination simulation method based on theoretical analysis and probabilistic iteration. The performance of CLYC was compared to that of common detectors in terms of physical properties and detection efficiency. A double-particle pulsed neutron detection system for porosity determination was established, based on the count ratio of equivalent gamma rays from the range of 2.95-3.42 MeVee energy bins. Results showed that CLYC can effectively replace ³He-tubes for porosity measurement, providing consistent responses. This study offers numerical simulation support for the design of future neutron well logging tools and the application of double-particle detectors in logging systems.

© 2025 The Authors. Publishing services by Elsevier B.V. on behalf of KeAi Communications Co. Ltd. This is an open access article under the CC BY-NC-ND license (http://creativecommons.org/licenses/by-nc-nd/4 0/).

1. Introduction

In borehole geophysics, neutron well logging using controllable source (e.g., D-D and D-T accelerator) or chemical source (e.g., Am-Be, Pu-Be, and ²⁵²Cf) is widely applied to determine oil saturation, differentiate lithology, estimate porosity and evaluate fluid properties, as well as monitor water injection performance, by recording gamma ray energy spectra, gamma ray time spectra or thermal neutron time spectra (Rider, 1986; Hearst and Nelson, 1985). The growing demands for unconventional oil and gas

resource assessment, CCUS (carbon capture, utilization, and storage), and EOR (enhanced oil recovery) in cased wells have driven the development of multifunctional neutron well logging (Kim and Akang, 2024; Machicote et al., 2023; Guo et al., 2024; Fan et al., 2021). To support the multifunctional capability of pulsed neutron logging, detectors must endure harsh downhole environments, including high temperatures, limited space, and strong vibrations, while detecting various types of particles simultaneously.

Breakthroughs in detection technology are essential for the advancement of neutron well logging. Detectors with high detection efficiency, temperature tolerance, and energy resolution remain key development goals in neutron well logging. In 1941, Pontecorvo pioneered a neutron-gamma logging system utilizing mesothorium, polonium, or radium combined with beryllium as neutron sources. The system employed an ionization chamber

E-mail address: zhfxy_cn@upc.edu.cn (F. Zhang).

Peer review under the responsibility of China University of Petroleum (Beijing).

^{*} Corresponding author.

Q.-X. Liang, F. Zhang, J.-T. Fan et al.

Petroleum Science 22 (2025) 4052–4064

filled with high-pressure argon to record the total gamma ray counts produced by thermal neutron capture reactions. As the first successful implementation of neutron-gamma logging, it was used to evaluate cement bonding integrity in wellbores (Pontecorvo et al., 1941). In the following decade, neutron-gamma logging was primarily employed to determine formation porosity. In the early 1950s, the development of scintillation detectors and the introduction of photomultiplier tubes enabled Tittman and Nelligan to demonstrate the feasibility of pulsed neutron spectroscopy logging in laboratory (Tittman and Nelligan, 1960). Neutroninduced gamma ray spectroscopy logging, exemplified by Carbon/Oxygen (C/O) logging, realized quantitative oil saturation determination though analyzing the count ratio of gamma rays (Hoyer and Rumble, 1965). With technological advancements, high-performance detectors such as CsI (Youmans et al., 1964), NaI (Schultz and Smith, 1974), GSO (Scott et al., 1991), and BGO (Beals et al., 1993) were incorporated into neutron spectroscopy logging to enhance the accuracy of saturation evaluation and improve continuous logging capabilities. Advancements in multichannel analyzers and scintillation detectors have made it feasible to quantitatively evaluate the elemental composition of subsurface formations. In 1996, the first geochemical logging tool, known as the Elemental Capture Spectroscopy Sonde (ECS), was introduced. Equipped with a large BGO detector, it marked the beginning of commercial application in formation elemental content evaluation (Herron and Herron, 1996). Subsequently, high-resolution and high-efficiency scintillation detectors, such as LaBr₃ (Odom et al., 2008), LaCl₃ (Odom et al., 2013), and YAP (Rose et al., 2015), were incorporated into neutron well logging to enhance the accuracy of elemental content, hydrocarbon saturation and bulk density evaluations (Wang et al., 2020, 2022). In 1951, Tittle utilized ³He-filled ionization chambers in neutron well logging, recording neutrons from a Ra-Be source as it traversed an artificially water-saturated sandstone formation. This experiment laid the foundation for the development of neutron-neutron well logging (Tittle et al., 1951). By the late 1950s, neutron-neutron well logging instruments employed Am-Be sources and ³He-filled Geiger-Mueller tubes had successfully commercial application. These instruments relied on thermal or epithermal neutron information to evaluate formation porosity and gas saturation. However, due to the scarcity of ³He gas, alternative neutron detectors, such as ⁶Li-loaded glass (Schneider and Hubner, 1991), BF₃, and ¹⁰B lined tubelets (Tsorbatzoglou and McKeag, 2011), were subsequently introduced in neutron-neutron well logging, aiming to replace ³He-tubes.

With advances in detection technology, elpasolite crystals with structural composition A₂BMX₆ such as Cs₂LiYCl₆:Ce(CLYC), Cs₂LiLaCl₆:Ce(CLLC), Cs₂LiYBr₆:Ce(CLYB), and Cs₂LiLaBr₆:Ce(CLLB), have attracted growing interest due to their excellent performance as gamma ray and neutron detectors (Combes et al., 1999; Bessiere et al., 2004; Van Loef et al., 2002). These crystals have attracted the focus of application research such as explosive detection, miniaturization of nuclear detection equipment, and other fields (Budden et al., 2015; Smith et al., 2013; Jin et al., 2022). In particular, their ability to simultaneously detect gamma rays and neutrons make them highly promising for environmental monitoring applications (Pérez-Loureiro et al., 2021; Zhao et al., 2023). As a representative double-particle detectors, CLYC demonstrates energy resolution comparable to that of LaBr₃ detectors (3.6% at 0.662 MeV) (Glodo et al., 2013; Bessiere et al., 2005) and excellent temperature tolerance (operating from -30 °C to 180 °C) (Yang and Menge, 2015). It also exhibits high light yield (the light output efficiency of gamma ray and neutron is 20000 photons/ MeV and 70500 photons/MeV), sharp roll-off, and high detection efficiency (24% for gamma rays and nearly 100% for thermal

neutrons) (Bessiere et al., 2005; Van Loef et al., 2005). These characteristics enable CLYC detectors to provide additional particle information in neutron well logging under the existing instrument structures. Furthermore, the simultaneous recording of neutron and gamma ray fields at the same depth interval reduces environmental interference, offering a more detailed description of neutron-nucleus interactions. The CLYC detector introduces novel approached for particle detection and holds the potential to advance neutron well logging into a new stage.

The use of advanced detectors to collect neutron-neutron and neutron-gamma information, which reflect slowing-down behavior and interaction characteristics of formation nuclei is essential for advancing and applying neutron based double-particle logging technology. Numerical simulation of double-particle responses forms the basis for integrating CLYC detectors into neutron logging systems. Monte Carlo based simulation program such as GEANT4, MCNPX, and MCNP6 have been widely used to generate double-particle responses under the laboratory conditions (Machrafi et al., 2014, 2015; D'Olympia et al., 2013; Glodo et al., 2013; Chowdhury et al., 2014; Lee et al., 2012). These programs enable detailed analysis of neutron transport, capture, and subsequent gamma ray production, providing critical insights into the interaction processes between neutrons and formation nuclei.

This study employed the open-source Monte Carlo numerical simulation program FLUKA, through modifications to selected source codes, enabled the generation of charged particles and the deposition of equivalent energy. By combining theoretical derivations with experimental results from publicly available literature, an innovative pulse shape discrimination spectrum simulation method based on probability iteration was proposed. Although pulse shape spectrum simulation is typically overlooked in standalone gamma ray or thermal neutron detection, it plays an essential role in double-particle detection systems. A CLYC based double-particle detection system was established within the framework of a compensated neutron porosity logging instrument, using a dualdetector system for downhole applications. Numerical simulations validated the feasibility of replacing existing ³He-tube with CLYC detectors. This work established the foundation for the downhole application of CLYC detectors and offered simulation method for the next generation of neutron well logging technology research.

2. Method and theory

As shown in Fig. 1, during the operation of neutron well logging instruments, fast neutrons emitted from the source undergo inelastic and elastic scattering with formation nuclei, gradually slowing down to thermal neutrons while releasing inelastic scattering gamma rays. Thermal neutrons are subsequently interacting with the nuclei by capture reactions, producing capture gamma rays. As the gamma rays propagate through the formation, they are attenuated by Compton scattering, photoelectric effect and pair production.

Based on the distinct interaction mechanisms of neutrons and gamma rays with formation nuclei, simultaneous detection of both particles enables a more comprehensive characterization of nuclear interactions, facilitating the evaluation of multiple formation properties within a single measurement. Additionally, detecting particles at the fixed spacing allows for a simplified description of neutron-gamma ray field distribution in both the borehole and surrounding formation, offering new insights into self-compensating corrections for environmental effects on the logging response.

Neutron interactions with formation nuclei can be described using the time-independent Boltzmann transport equation, as given in Eq. (1) (Lewis and Miller, 1984).

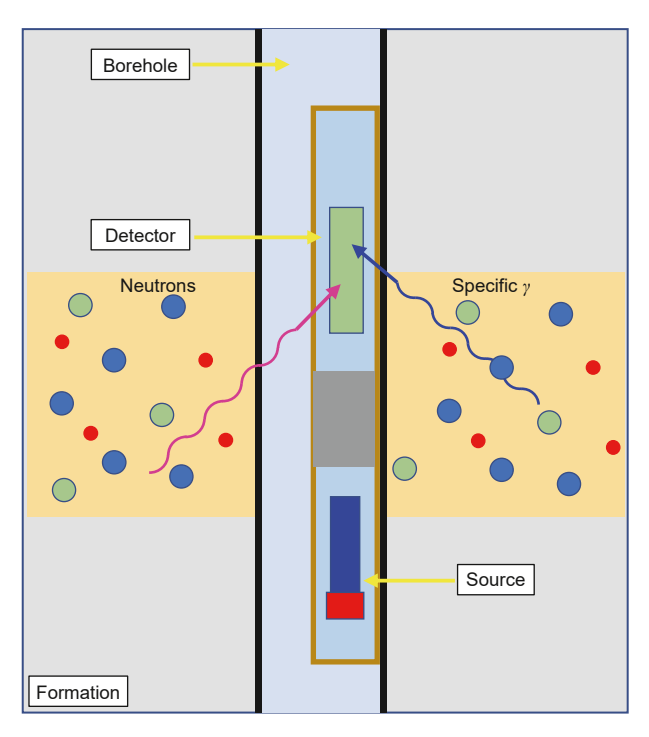


Fig. 1. Schematic diagram of double-particle detection in neutron well logging.

$$\begin{split} \Omega \cdot \nabla \Phi(r,E,\Omega) + \Sigma_t \Phi(r,E,\Omega) &= \int d\Omega' \int dE' \Sigma_s(r,E'\Omega' \to E\Omega) \\ \Phi(r,E',\Omega') + q(r,E,\Omega) \end{split} \tag{1}$$

where Ω represents direction vector of the incident particle. $\Phi(r, E, \Omega)$ represents the angular flux at distance of r with energy E and direction Ω . Σ_t represents the macroscopic neutron scattering cross section or linear absorption coefficient at locate \overrightarrow{r} . Ω' represents direction vector of the scattering particle. E' is energy of scattering particle. The source intensity, $q(r, E, \Omega)$ is an isotropic point source emitted uniformly in all directions (360°).

Based on the Boltzmann transfer equation, the thermal neutron flux distribution in an infinite homogeneous medium at a distance r can be further derived using the two-group diffusion theory (Tittle, 1961).

$$\Phi_{t}(r) = \frac{S_{o}}{4\pi D_{t}r} \frac{L_{t}^{2}}{L_{f}^{2} - L_{t}^{2}} e^{-r/L_{f}}$$
(2)

where $L_{\rm f}$ represents the fast neutron slowing-down length, $L_{\rm t}$ is the thermal neutron diffusion length, and $D_{\rm t}$ is the thermal neutron diffusion coefficient.

As shown in Eq. (2), thermal neutron flux is influenced by the processes of slowing down, diffusion, and neutron capture. Compensated neutron porosity logging utilizes the ratio of thermal neutron counts from near to far spacing to minimize the influence of borehole environment. Given that the diffusion length is significantly shorter than the slowing-down length, the counts ratio of thermal neutron primarily reflects the slowing down behavior. Since the slowing-down length is strongly dependent on the hydrogen index, making the ratio is possible to determine formation water-filled porosity. However, because different lithologies exhibit distinct slowing-down lengths, lithology correction is essential in compensated neutron porosity logging. Compared to formation fluids, rock matrix components are more

diverse and exhibit a wide range of mineral compositions. These variations result in substantial differences in neutron characteristic lengths and cross sections. By quantifying the elemental composition, the mineral content and type of the formation can be inferred, thereby improving the accuracy of porosity evaluation.

In scintillator-based nuclear detection, gamma rays generated by neutron interactions with the surrounding medium are not directly measured. These gamma rays interact with detector material and produce secondary charged particles. Through subsequent processes including ionization, scintillation, and photoelectric amplification, electrical signals are generated and processed. The resulting pulse heights are then sorted by a multichannel analyzer to construct an energy spectrum. As shown in Eq. (3), the measured gamma energy spectrum $N(E_{\rm d})$, depends on three factors: the characteristic gamma rays $\Phi_{\rm E}$, the interaction between gamma rays and the detector material R_1 , and the energy transformations including ionization, scintillation, photoelectric amplification, and signal processing, represented by R_2 (Borella et al., 2018).

$$N(E_{\rm d}) = \iiint R_2(E_{\rm d}, E_{\rm e}) R_1(E_{\rm e}, E_{\gamma}, \overrightarrow{r}) \Phi_{\rm E}(E_{\gamma}, \overrightarrow{r}) dE_{\rm e} dE_{\gamma} d\overrightarrow{r}$$
(3)

where $N(E_{\rm d})$ represents the observed gamma ray counts. E_{γ} is the energy of incident gamma rays. $E_{\rm e}$ is the energy of electron generated through the interaction between specific gamma rays and the detector material. The function $R_1(E_{\rm e}, E_{\gamma}, \overrightarrow{r})$ describes the interaction of characteristic gamma rays with the detector material, which can be simulated by the Monte Carlo method. The function $R_2(E_{\rm d}, E_{\rm e})$ describes the energy deposition from fluorescence to the scintillator, which can be approximated in a Gaussian function. Both R_1 and R_2 depend solely on the intrinsic characteristics of the detector and can be determined through a combination of numerical simulations and crystal property measurements.

As the key element for thermal neutron detection, lithium in the CLYC detector interacts with thermal neutrons through $^6\text{Li}\ (n,t)\alpha$ reaction as shown in Eq. (4). This reaction has a thermal neutron capture cross section of 940 b and a Q-value of 4.78 MeV. During the interaction, energy is deposited in the form of 2.05 MeV α -particle and 2.73 MeV ^3_1H -particle, resulting in a distinct full-energy peak in the measured spectrum.

$$n + {}_{3}^{6}Li \rightarrow {}_{2}^{4}He + {}_{1}^{3}H + 4.78MeV$$
 (4)

Similar to gamma ray detection, the neutron-induced energy spectrum $N'(E_d)$ also depends on the energy transformation processes within the detector. An additional step must be incorporated to account for the neutron interaction with the detector material, which modifies the original gamma flux distribution $\Phi_E(E_\gamma, \overrightarrow{r})$ into an equivalent gamma ray flux $\Phi'_F(E'_\gamma, \overrightarrow{r})$.

When particles enter the CLYC detector, visible light fluorescence is produced through two luminescence mechanisms: Core to Valence Luminescence (CVL) and Self-trapped Exciton Luminescence (STE). STE occurs under the incidence for any particle and is associated with a slower luminescence process. In contrast, the case of gamma ray incidence primarily produces CVL fluorescence, characterized by the very fast decay time (~2 ns). Fig. 2 shows the idealized pulse shape spectrum based on the experiment of D'Olympia et al. (2013). Both CVL and STE occur on a nanosecond timescale, the differences in luminescence behavior between gamma rays and thermal neutrons are less distinguishable on the microsecond timescale. Overall, the normalized pulse shape of gamma ray events is similar in profile to that of thermal neutrons but exhibits a lower amplitude. Fig. 3 further illustrates this behavior by zooming in on the pulse amplitude spectrum in the

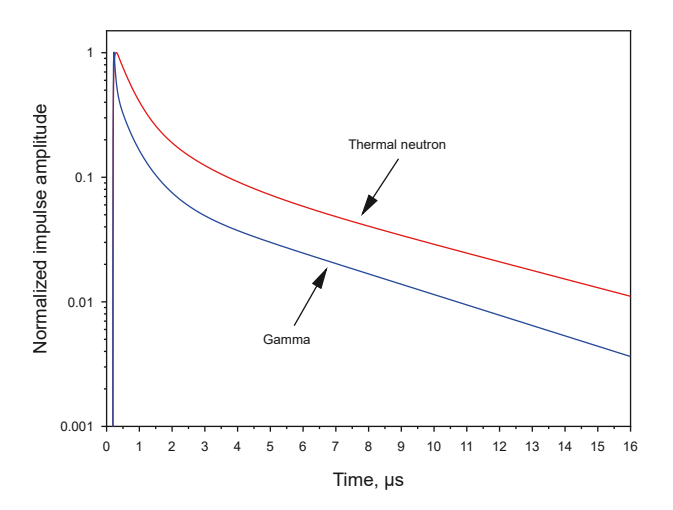


Fig. 2. Normalization of the cumulative pulse shape spectrum under experiment.

200–350 ns range. In the highlighted yellow region, the rapid rise and decay associated with CVL under gamma ray excitation is clearly observed, while thermal neutrons exhibit a more gradual increase, indicative of the STE-dominated response.

Pulse shape discrimination (PSD) techniques, such as the Charge Integration Method, Rise Time Analysis Method, Peak-to-Tail Ratio Method, and Pulse Width Analysis Method, classify incident particle types based on temporal characteristics of their pulse signals (e.g., rise time, fall time, or total duration). In this study, the Charge Integration Method is used to distinguish the type of incident particles.

Two integration windows are defined by segmenting the pulse shape spectrum: the initial rising portion is defined as the prompt window, while the subsequent decaying portion is defined as the delayed window. Eq. (5) presents the formula for calculating the PSD value, which is defined as the proportion of the delayed window counts to the total counts in both delayed and prompt windows. The total counts in the prompt and delayed windows are denoted as Q_{prompt} and $Q_{delayed}$, respectively. The width of the delayed and prompt windows can be optimized by traversing the pulse shape spectrum to identify the optimal figure of merit (FOM) for the best discrimination quality.

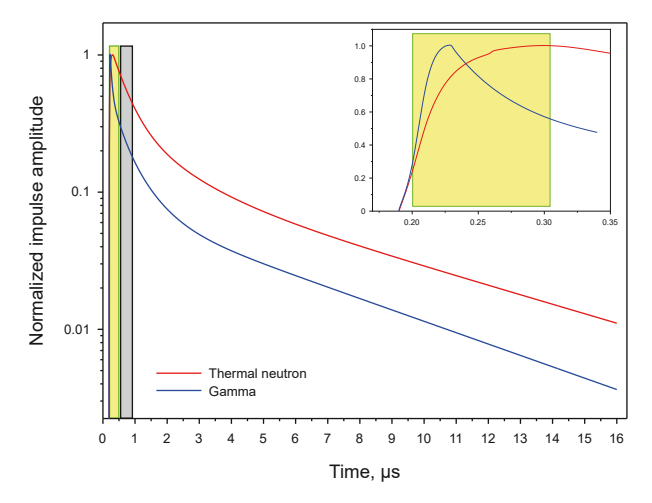


Fig. 3. Results of pulse shape discrimination time window division.

$$PSD = \frac{Q_{delayed}}{Q_{delayed} + Q_{prompt}}$$
 (5)

The pulse shape spectrum consists of multiple decay components with exponential decay characteristics from various luminescence mechanisms. Consequently, the pulse shape spectra generated by incident thermal neutrons and gamma rays can be distinguished using a multi-exponential summation model. Fig. 4 (a), (b) display the classification results of normalized pulse shapes under different particle incidence conditions. For thermal neutrons, the spectrum is characterized by three components, as described in Eq. (6). Due to the presence of the CVL mechanism, gamma rays are characterized using four components, as described in Eq. (7).

Incident thermal neutron pulse shape calculation formula:

$$A_{n}(t) = A_{n0}e^{\frac{-t}{r_{1}}} + A_{n1}e^{\frac{-t}{r_{2}}} + A_{n2}e^{\frac{-t}{r_{3}}}$$

$$\tag{6}$$

Incident gamma ray pulse shape calculation formula:

$$A_{g}(t) = A_{g0}e^{\frac{-t}{r_{1}}} + A_{g1}e^{\frac{-t}{r_{2}}} + A_{g2}e^{\frac{-t}{r_{3}}} + A_{g3}e^{\frac{-t}{r_{4}}}$$
(7)

where τ represents the specific values for different attenuation coefficients as shown in Table 1. Ais represented as the initial pulse shape value for different constituents.

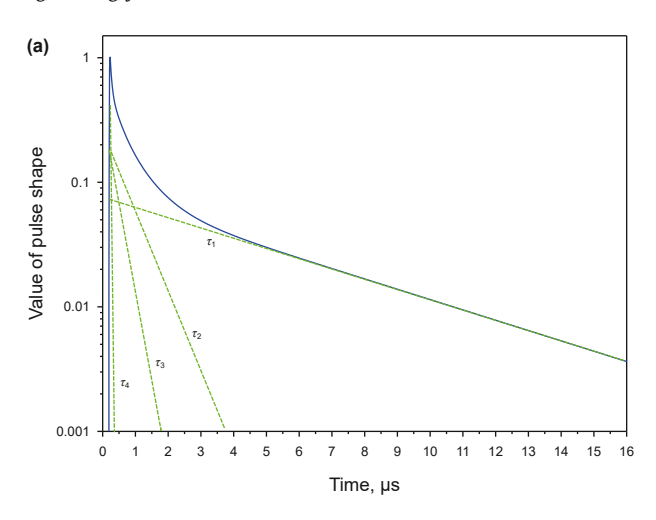
According to the experimental results of N. D'Olympia, Kan Yang, and Jarek Glodo, the PSD value for gamma rays in the two-dimension pulse shape discrimination spectrum (2D-PSD) remains relatively stable as the incident energy increases, while the distribution area expands significantly in the low-energy region (D'Olympia et al., 2013; Yang and Menge, 2015; Glodo et al., 2013). Wen and Enqvist (2017) conducted experiments using monoenergetic gamma rays at energy of 200, 300, 400, 500, 662, 700, 800, and 900 keV. As shown in Table 2, the proportion of the delayed luminescence component gradually increases with higher incident energy. This phenomenon is primary attributed to the changes in decay constant τ . On the other hand, thermal neutrons, which deposit relatively constant energy, exhibit a stable proportion of the delayed component, resulting in a consistent 2D-PSD distribution.

The temporal variation patterns of the initial amplitudes and decay constants for each exponential component under different energy conditions have been established. By introducing energy-dependent correction functions into both the amplitude and decay constant terms, the improved pulse shape spectrum can be calculated using Eqs. (8) and (9).

$$A_n(t) = \sum_{i=1}^{3} A_{n_i}(E) e^{\frac{-t}{rn_i(E)}}$$
 (8)

$$A_{g}(t) = \sum_{i=1}^{4} A_{g_{i}}(E) e^{\frac{-t}{r_{g_{i}}(E)}}$$
(9)

As shown in Eq. (3), the Monte Carlo numerical simulation method is employed to determine the particle type and count rate enter the detector. The charged particles generated from the interaction between incident particles and the detector material correspond to R_1 . By incorporating actual measurements speed of instrument, source intensity, and size of detector, the simulation results can be converted into actual counts. The equivalent gamma ray counts within the specific energy channels are then used to define the number of iterations for pulse shape spectrum under different particle incidence conditions. The calculation formulas for gamma ray and thermal neutron pulse shape spectra are provided in Eqs. (11) and (12).



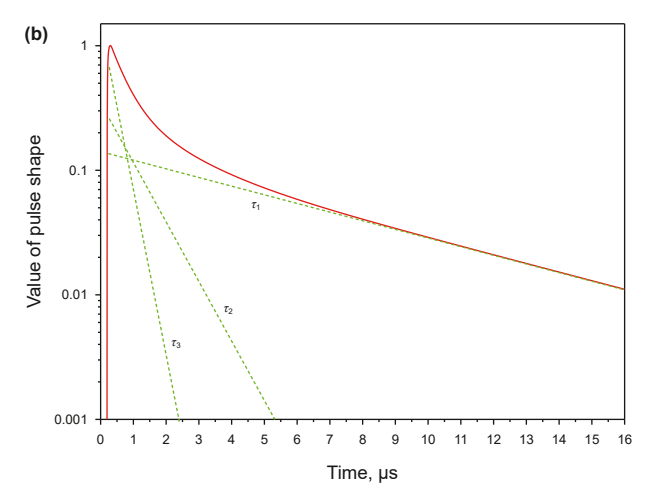


Fig. 4. Normalized pulse shape division results under condition of different particles incidence. (a) Gamma ray. (b) Thermal neutron.

Table 1
Decay life of luminescence components (D'Olympia et al., 2013).

Particle type	τ _{1,} μS	τ _{2,} μS	τ3, μS	τ _{4,} μS
Thermal neutron	6.03 ± 0.04	1.42 ± 0.04	0.45 ± 0.01	_
Gamma ray	5.24 ± 0.03	0.73 ± 0.04	0.28 ± 0.03	0.048 ± 0.004

By introducing energy-dependent properties and accounting for measurement uncertainties, the specific values of the attenuation coefficients are determined as follows:

$$\tau = u(E) \pm \overline{v} \tag{10}$$

Incident thermal neutron pulse shape calculation formula:

$$A_{n}(t) = \sum_{i=1}^{3} A_{n_{i}}(E) e^{\frac{-t}{u(E)g_{i}}} + X(t) \cdot \sum_{i=1}^{3} A_{n_{i}}(E) e^{\frac{-t}{u(E)g_{i}}} \frac{t}{u(E)_{n_{i}}^{2}} \overline{v_{i}}$$
 (11)

Incident gamma ray pulse shape calculation formula:

$$A_{\mathbf{g}}(t) = \sum\nolimits_{i=1}^{4} A_{\mathbf{g}_{i}}(E) \mathrm{e}^{\frac{-t}{u(E)\mathbf{n}_{i}}} + X(t) \cdot \sum\nolimits_{i=1}^{4} A_{\mathbf{g}_{i}}(E) \mathrm{e}^{\frac{-t}{u(E)\mathbf{g}_{i}}} \frac{t}{u(E)_{\mathbf{g}_{i}}^{2}} \overline{v_{i}} \qquad (12)$$

where *X* represents the noise factor, the value is -1 to 1, meeting the Gaussian normal distribution of a certain half-height width $N\left(0, \left(\frac{FWHM}{2.355}\right)^2\right)$.

3. Monte Carlo simulation

FLUKA (FLUktuierende KAskade) is a Monte Carlo simulation code jointly developed by the Italian National Institute for Nuclear Physics (INFN) and the European Organization for Nuclear Research (CERN). It is employed to simulate over 60 types of particles transport processes and has been widely used in applications such as detector design, cosmic ray detection, neutrino physics, and radiation therapy (Battistoni et al., 2015). In this study, FLUKA is utilized to simulate the neutron and gamma ray responses in the CLYC detector by collecting information on charged particles generated from interactions, along with corresponding energy deposition results. By integrating the simulation results with experimental data, a pulse shape spectrum simulation based on probability iteration is developed. To ensure the reliability of the numerical simulation, comparisons are made with experimental results published in some open literatures.

3.1. Numerical simulation of detector response as gamma ray incidence

In the numerical simulation of gamma ray incidence conditions, the experimental results by Jianguo Qin are referenced (Qin et al., 2018). The FLUKA numerical simulation model is established as shown in Fig. 5, which consists of a cylindrical CLYC detector placed in air, with crystal dimensions of $\phi 1"\times 1"$, enclosed in an aluminum shell with a density of 3.31 g/cm³. The crystal is enriched 95% ^6Li and 0.5 mol% Ce $^{3+}$. A ^{60}Co isotopic source emitting isotropically, is positioned 2 cm above the detector. "DETECT" card is employed to record the energy deposition from the ^{60}Co source, while the "DETGEB" card is employed to set the detector's energy resolution to 4.48% (at 662 keV), matching the performance of the actual detector.

Compared the results between experiment and simulation, the full-energy peaks (FEPs) at 1173 keV and 1332 keV exhibit good agreement with the experiment. The main discrepancies are

Table 2The decay time and fraction coefficient of each component for different energy depositions by gamma rays in the CLYC detector (Wen and Enqvist, 2017).

Energy, keV	$\tau_{1,}$ ns	$\frac{A_1}{\tau_1} \times 10^{-5}$	τ _{2,} ns	$\frac{A_2}{\tau_2} \times 10^{-5}$	τ _{3,} ns	$\frac{A_3}{ au_3} \times 10^{-5}$	τ _{4,} ns	$\frac{A_4}{\tau_4} \times 10^{-5}$
190–210	0.242 ± 0.005	5.18 ± 0.03	47.0 ± 0.6	2.93 ± 0.01	651 ± 8	24.2 ± 0.2	4955 ± 65	72.9 ± 0.2
290-310	0.374 ± 0.006	5.44 ± 0.03	50.0 ± 0.5	3.36 ± 0.02	667 ± 6	24.3 ± 0.1	5041 ± 53	72.3 ± 0.2
390-410	0.206 ± 0.007	2.09 ± 0.03	51.9 ± 0.4	3.70 ± 0.02	677 ± 5	24.4 ± 0.1	5077 ± 49	71.9 ± 0.1
490-510	0.169 ± 0.006	1.33 ± 0.02	52.7 ± 0.4	3.71 ± 0.02	685 ± 5	24.5 ± 0.2	5138 ± 52	71.8 ± 0.2
652-672	0.228 ± 0.005	1.12 ± 0.07	53.4 ± 0.2	3.83 ± 0.03	687 ± 5	24.6 ± 0.1	5127 ± 44	71.6 ± 0.1
790-810	0.125 ± 0.004	0.34 ± 0.07	53.9 ± 0.3	4.22 ± 0.03	692 ± 6	24.5 ± 0.1	5163 ± 52	71.3 ± 0.2
890-910	0.128 ± 0.006	0.22 ± 0.07	54.4 ± 0.2	4.34 ± 0.05	689 ± 6	24.5 ± 0.1	5144 ± 55	71.2 ± 0.2
990–1010	0.096 ± 0.003	0.05 ± 0.07	54.6 ± 0.2	4.39 ± 0.05	690 ± 6	24.4 ± 0.1	5152 ± 55	71.2 ± 0.2

Q.-X. Liang, F. Zhang, J.-T. Fan et al. Petroleum Science 22 (2025) 4052–4064

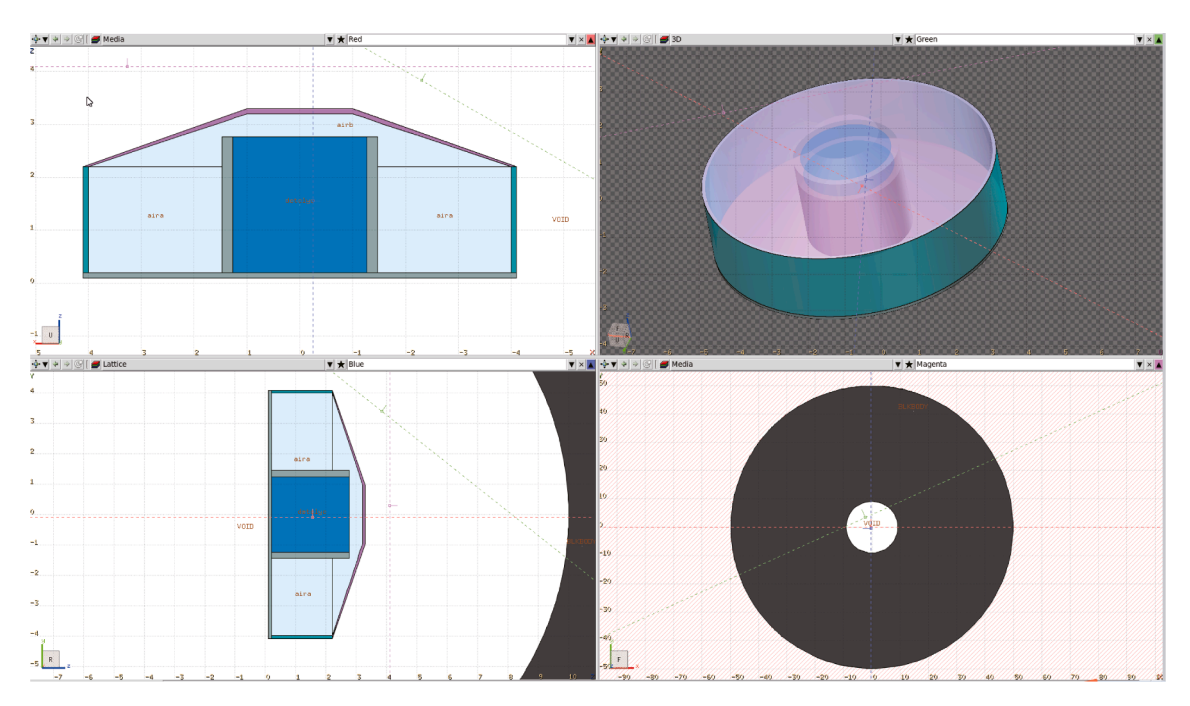


Fig. 5. Establishment of FLUKA numerical simulation model.

observed in the multiple Compton events, the Compton continuum, and the energy peaks at 32 keV and 218 keV. The 32 keV peak corresponds to the bremsstrahlung X-rays of the incident particles, while the 218 keV peak represents the backscattering peak of gamma rays. These discrepancies are primarily attributed to limitations in the original numerical model. In this study, based on the original model, an additional 1 cm thick tungsten shield was added to improve the accuracy of low-energy numerical simulation results. As shown in Fig. 6. With this adjustment, the simulated Compton continuum and full-energy peaks align well with the experimental data. Moreover, the positions of the backscattering and bremsstrahlung peaks in the simulation also correspond well with the experimental observations.

The broadening of the energy spectrum recorded by the detector is influenced not only by the intrinsic properties of the

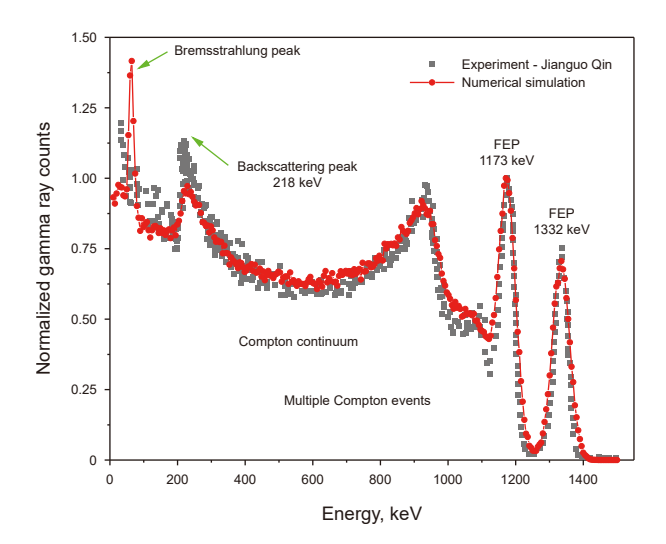


Fig. 6. Comparison of numerical simulation and experimental results of $^{60}\mathrm{Co}$ detection response.

scintillator material but also by external factors such as the crystal growth quality, photomultiplier tube (PMT), and multi-channel analyzer resolution. As a result, each detector exhibits slight variations in detection performance and measured energy spectra, while current numerical simulation software overlooks that. Such software commonly models energy resolution by shaping the full-energy peak based on a fixed resolution function and defining the peak range using known characteristic gamma ray energies. This simplification can introduce discrepancies between simulated and measured spectra. In the case of downhole neutron-gamma energy spectral measurements, low-energy features such as back-scattering and bremsstrahlung peaks are always overshadowed by high-energy Compton contributions. Therefore, discrepancies in the low-energy regions are always ignored.

3.2. Numerical simulation of detector response as thermal neutron incidence

To further investigate the energy deposition characteristics of the CLYC detector under thermal neutron incidence, this study refers to the experimental simulation reported by Machrafi et al. (2015). The instrument model consists of a cylindrical detector placed in air, with a radius and height set to 2.5 cm each, Crystal material is Cs₂LiYCl₆:Ce³⁺, with a gamma ray energy resolution of 6.9% (662 keV), while the thermal neutron measurement equivalent gamma ray energy resolution is 3.3%. A monoenergetic and isotropic ¹³⁷Cs point source emitting 662 keV gamma rays is used to calibrate the channel-energy relationship. Additionally, the Am-Be neutron source is positioned above the detector and enclosed in a cylindrical paraffin container with a thickness of 4.5 cm, ensuring the fast neutrons are moderated to thermal neutrons. Two measurements were conducted: the first measurement was to calibrate the channel position using both the ¹³⁷Cs and the moderated Am-Be source simultaneously, and the second measurement involved the moderated Am-Be source alone to observe the thermal neutron response.

FLUKA is employed to perform numerical simulations, and the overall workflow is illustrated in Fig. 7. The numerical simulation is

Q.-X. Liang, F. Zhang, J.-T. Fan et al.

Petroleum Science 22 (2025) 4052–4064

divided into two main parts, "physical structure & source definition" and "neutron & gamma ray recording". In this section, simultaneous simulations of gamma rays and thermal neutrons are conducted, consistent with the subsequent formation response acquisition simulations, which are described in detail herein. Neutron and gamma sources defined user-defined routine *Source*. f. The "PHYSICS", "LOW-NEUT", and "LOW-MAT" cards are activated to enable low-energy neutron transport, while "USER-WEIGHT" and "DETECT" cards are employed for recording simulation data. To enable detailed analysis of energy deposition, the routine *comscw. f* is modified to separately record the energy deposition of alpha and tritium, which generated from the interaction of thermal neutrons with lithium in the CLYC detector.

Comparison between numerical simulation and experimental results is shown in Fig. 8. Since a gamma ray source was used for neutron energy calibration, the X-axis is set to equivalent gamma energy, expressed in MeVee. As shown in Eq. (4), thermal neutrons interact with ⁶Li in the detector produce alpha particles with an energy of 2.05 MeV and tritons $\binom{3}{1}H$) with an energy of 2.73 MeV, resulting in a total energy deposition of 4.78 MeV. However, as illustrated by the pink line in Fig. 8, the experimental spectrum exhibits peaks at 0.19, 0.662, and 3.24 MeVee. Specifically, the 0.19 MeVee peak corresponds to the backscattering peak of ¹³⁷Cs, the 0.662 MeVee peak represents the full-energy peak of ¹³⁷Cs, and the 3.24 MeVee peak corresponds to the equivalent gamma ray energy deposition from thermal neutron. The experimental results indicate that the equivalent gamma ray energy deposited by secondary charged particles generated through thermal neutrons interactions is influenced by the conversion efficiency, which is determined to be approximately 67%.

The red line in Fig. 8 represents the thermal neutron energy deposition spectrum obtained from FLUKA simulation. The numerical simulation results align with the theoretical expectation,

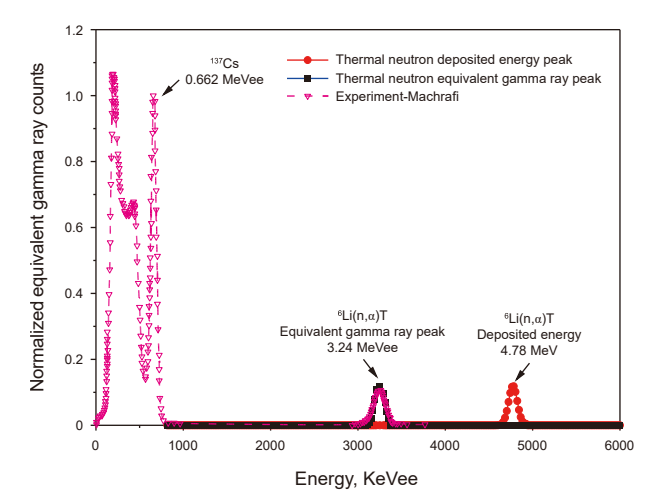
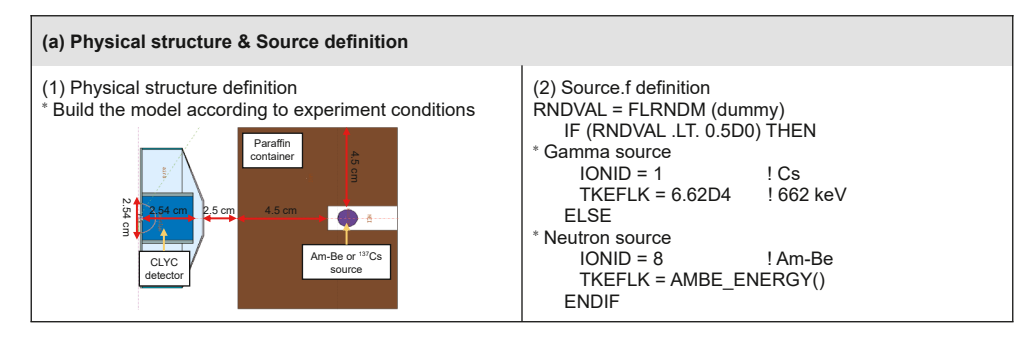


Fig. 8. Comparison of numerical simulation and experimental results for the detector response to ¹³⁷Cs and moderated Am-Be sources.

showing a deposited energy of 4.78 MeV. However, a 1.54 MeV energy discrepancy is observed when compared to the equivalent gamma ray energy deposition measured experimentally. This discrepancy is attributed to energy loss during the scintillation process in the detector crystal. In FLUKA, no dedicated input card exists to account for the quenching effect, which leads to an overestimation of the deposited energy in the simulation. To address this, as show in Fig. 7 step b, the routine *comscw. f* and "DETECT" card were modified to simulate the equivalent gamma energy spectrum of thermal neutrons more accurately. The black line in Fig. 8 shows the converted thermal neutron equivalent



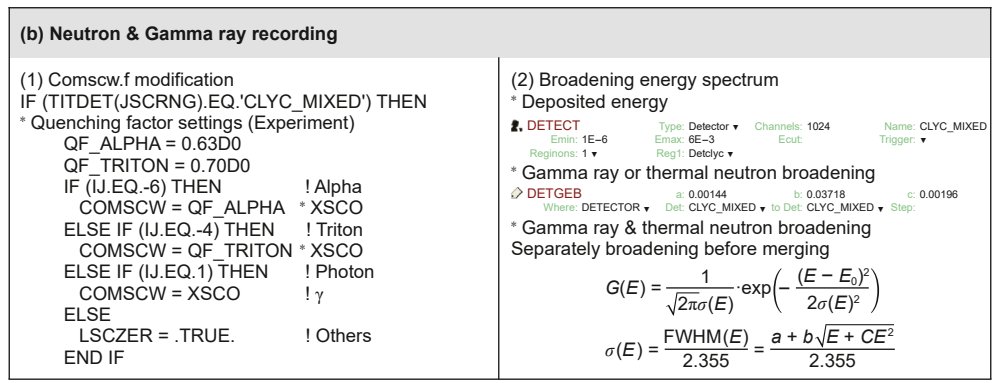


Fig. 7. The workflow of obtaining the equivalent gamma ray spectrum by FLUKA.

Q.-X. Liang, F. Zhang, J.-T. Fan et al.

Petroleum Science 22 (2025) 4052–4064

gamma energy spectrum, with peak of 3.24 MeVee consistent with the experimental observations.

3.3. Comparison of commonly used detector in neuron well logging

In addition to its neutron and gamma ray detection capabilities, the physical properties of the CLYC detector play a critical role in assessing its suitability for neutron well logging applications. Table 3 presents a comparison of the physical properties of commonly used scintillator detectors and two popular elpasolite crystals. The performance of the CLYC is comparable to that of LaCl₃, offering excellent temperature resistance and resistance to hydrolysis. Moreover, it possesses high mechanical and chemical strength. These properties make CLYC well-suited for deployment in high-temperature and high-pressure downhole environments.

Detection efficiency is another key factor in determining the suitability of scintillator detectors for neutron well logging. In this study, a scintillator detector with a size of $\varphi 1.5"\times 2"$ was placed in air, surrounded by a virtual spatial source within a 3 cm radius was defined to simulate gamma rays entering the detection range. To reflect the actual well logging situations, the source within the detection region was set as neutron induced gamma ray counts and thermal neutron counts recorded at the capture gate, under a water saturated sandstone formation with 10% porosity.

As shown in Table 4, NaI detectors, the most commonly used scintillator in nuclear logging, exhibit an absolute gamma ray detection efficiency of 36%. Due to the higher density compared to NaI, BGO and LaBr₃ achieve relative detection efficiency of 184% and 116%, respectively, under the same detector volume. In contrast, CLYC, with slightly lower density, yields a relative gamma ray detection efficiency of 87.5% compared to NaI. For thermal neutron detection, CLYC relies on the 6 Li (n,t) $_{\alpha}$ reaction, achieving a detection efficiency that surpasses that of 3 He-tubes.

3.4. Numerical simulation of porosity logging response

Building upon the conventional pulsed neutron gamma ray spectroscopy instrument, a novel pulsed neutron well logging system has been established by replacing the gamma ray detector with CLYC as show in Fig. 9. The near detector with a spacing of 30 cm and a size of φ 1.5" \times 2", and 55 cm for the far detector with a size of φ 1.5" \times 4". The outer diameter of the instrument is 43 mm. In this system, the burst gate is configured to operate within a 40- μ s timeframe, synchronized with the emission of fast neutrons from the D-T source. After a 10- μ s delay, the capture gamma rays are collected within a time span from 50 to 100 μ s.

A cased well with a columnar medium was constructed for analysis. The columnar medium has a height of 137 cm and a diameter of 70 cm. The borehole, with an internal diameter of 15.2 cm, is lined with a stainless steel casing 0.7 cm thick and filled

Table 4Detection efficiency comparison of common scintillator detectors and ³He tubes.

Scintillator	Absolutely detection efficiency, %		Relative detection efficiency, %	
	Total	Thermal neutron	NaI	³ He-tube
NaI(Tl)	36.8	~	100	~
BGO	67.8	~	184.2	~
LaBr ₃	42.7	~	116.0	~
CLYC(Ce) (95% ⁶ Li)	32.2	~100	87.5	111.1
³ He-tube (4 atm)	~	~90	~	100

with pure water. A 3 cm-thick calcium silicate cement ring reinforces the casing. The surrounding formation matrix consists of common minerals, including sandstone, limestone, dolomite and clay. The porosity of formation is varied within a range from 0% to 30%.

To illustrate a clearer explanation of the CLYC numerical simulation method in neutron well logging applications, the workflow of neutron-based double-particle logging is shown in Fig. 10. The process begins with the D-T source emitting fast neutrons, which interact with the formation medium to produce gamma rays and thermal neutrons. These particles are subsequently transported to the detector measurement zone, as described in Section 3.4.1. In the particle recording stage (Section 3.4.2), the CLYC response simulation method proposed in this study converts the specific gamma ray and thermal neutron information into pulse height spectra. Based on the recorded energy and time spectra, the corresponding count ratio parameters are extracted to evaluate formation porosity, as detailed in Section 3.4.3.

3.4.1. Field distribution of neutron-neutron and neutron-gamma ray

Neutrons interact with formation nuclei to produce induced gamma rays and thermal neutrons. As these particles are transported through the formation, neutron and gamma ray information eventually reaches the vicinity of the detector. Upon interacting with the detector material, the particles are recorded as energy spectra or time spectra data. Thus, before performing instrument response simulations, it is essential to first obtain the neutron-gamma and neutron-neutron field distribution incident on the detector. These field distributions serve as the foundation for accurately simulating the neutron well logging response.

Fig. 11(a) illustrates the distribution of neutron-induced gamma rays recorded within the detection zone during the capture gate. As porosity increases, the hydrogen content in the formation rises, resulting in enhancing gamma ray counts of hydrogen at 2.23 MeV. Simultaneously, reduced matrix content

Performance comparison of commonly used scintillator detectors.

Scintillator	Density, g/cm ³	Luminescence decay time, ns	Relative luminous intensity, %	Energy resolution, % (at 662 keV)	Temperature, °C	Delique -scence
NaI(Tl)	3.67	230	100	~6–7	-20~150	Yes
BGO	7.13	300	15–20	~10	-20~250	No
GSO	6.71	60	20-30	~7.9	-20~300	No
CsI(T1)	4.51	1000	45–55	~6	-20~200	Slightly
LaBr ₃	5.08	16	160	~2.8	-20~150	Yes
LaCl ₃	3.85	28	125	~3.2	-20~150	Yes
YAP	5.37	27	30	~5.5	-20~350	No
CLLB(Ce)	~5.1	40	~35	~4	-20~250	No
CLYC(Ce)	~3.3	100-300(γ) 1000-2000(n)	~50	~4	-20~200	No

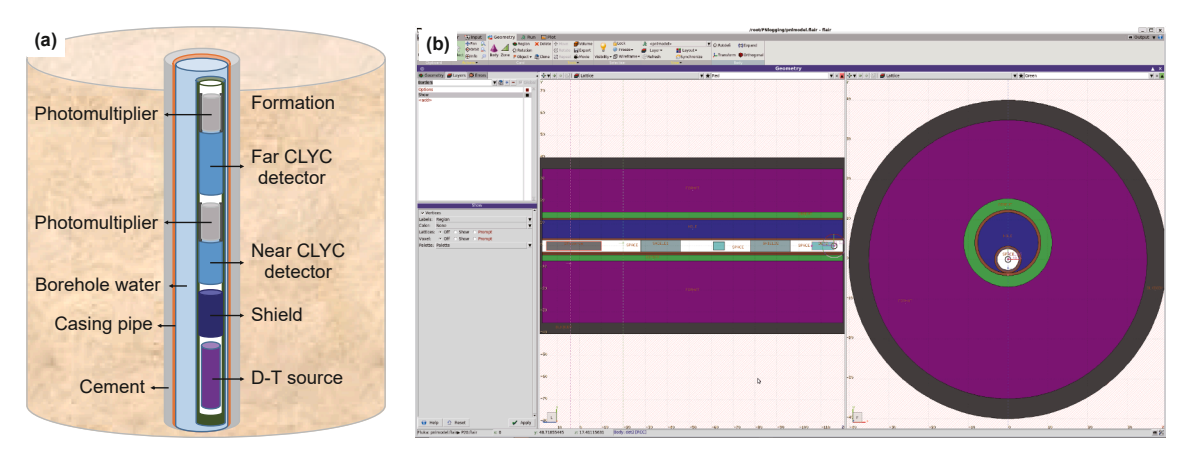


Fig. 9. Dual-CLYC pulsed neutron system. (a) Schematic diagram of double CLYC neutron well logging measurement system. (b) FLUKA numerical simulation model construction for double CLYC neutron well logging measurement system.

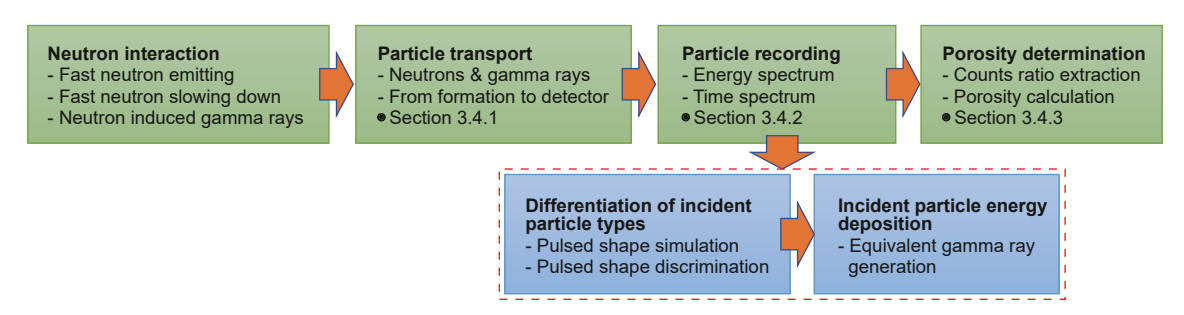


Fig. 10. The workflow to achieve the numerical simulation of porosity determination by Dual-CLYC pulsed neutron system.

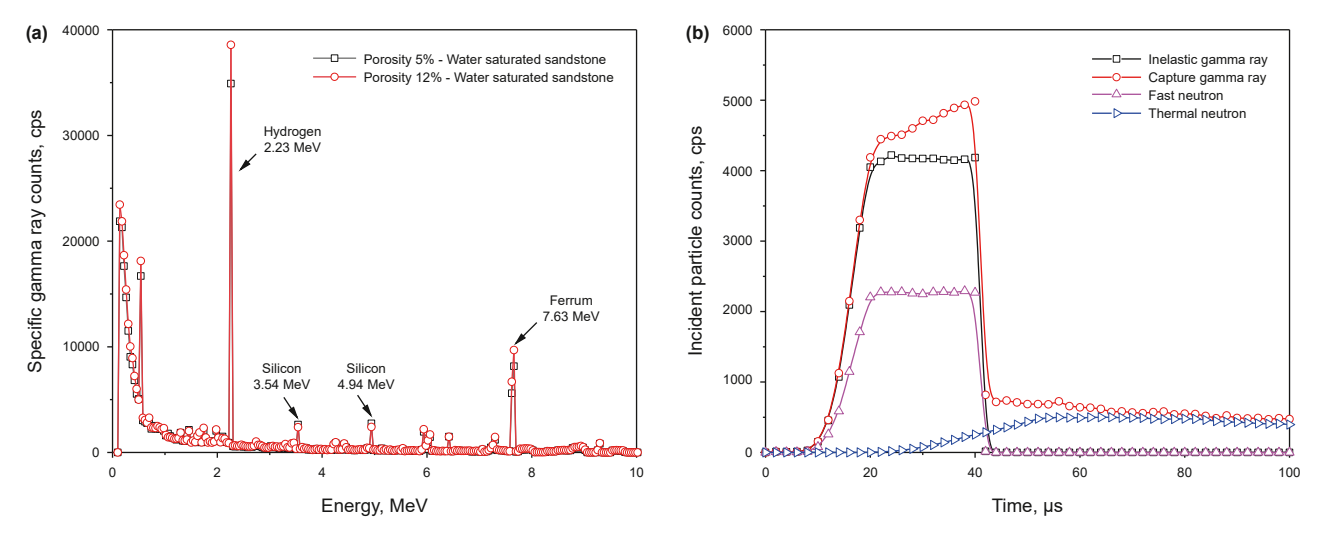


Fig. 11. The energy spectrum and time spectrum of incident particle within the zone of detector. (a) Specific gamma ray in detection zone. (b) Time spectrum in detection zone.

leads to decrease the gamma ray counts from silicon at 4.94 MeV and 3.54 MeV. Fig. 11(b) presents the neutron and gamma ray time spectra recorded in the detection zone during a short pulse period. Throughout the pulse emission cycle, fast neutrons are continuously emitted by the D-T source and subsequently moderated into thermal neutrons. Once the D-T source is turned off, the thermal neutron counts reach a peak before decaying over time as capture reactions occur within the formation. This time-dependent behavior reflects the dynamic interaction of neutrons with the

formation and their subsequent moderation and capture processes.

3.4.2. Logging response simulation of CLYC detector

(1) Detection response of pulsed shape spectrum

As neutrons or gamma rays interacting with the detector will generate distinct pulse shape spectra. Due to the statistical nature of nuclear detection, these spectra are subject to statistical Q.-X. Liang, F. Zhang, J.-T. Fan et al. Petroleum Science 22 (2025) 4052–4064

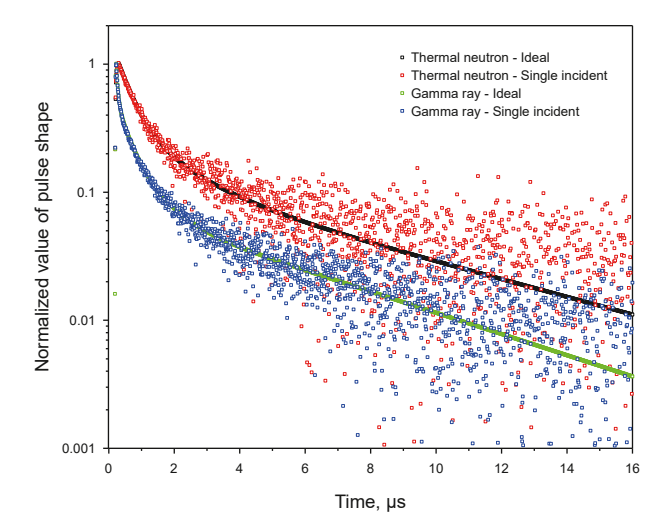


Fig. 12. The pulse shape spectrum generated from a thermal neutron or gamma ray incidence.

fluctuations. Using the pulse shape spectrum simulation method proposed in this study, the simulated pulse shape spectrum generated by the incidence of a single particle is presented in Fig. 12. Each neutron or gamma ray event produces a corresponding pulse shape spectrum, and based on the neutron-neutron and neutron-gamma ray counts recorded within the detection zone, the pulse shape discrimination (PSD) value for each event is calculated using Eq. (5). These calculation results in the two-dimensional PSD distribution (2D-PSD) shown in Fig. 13, which effectively distinguishing between neutron and gamma ray events.

As illustrated in Fig. 13, the 2D-PSD combines incident particle energy with the corresponding PSD value, thereby delineating distinct regions. PSD values around 0.7 are corresponding to thermal neutron count information, while the PSD values around 0.6 are corresponding to gamma ray. The separation between these PSD value clusters enables effective classification of incident particle types. Fig. 13(a) and (b) depict the 2D-PSD under different formation porosity conditions. In Fig. 13(a), the neutron counts are significantly higher than in Fig. 13(b), indicating that the detector recorded fewer thermal neutron counts under low-porosity reservoir conditions. In contrast, gamma ray counts remain

relatively consistent across both scenarios. Notably, the gamma ray counts at the 2.23 MeVee (hydrogen peak) in Fig. 13(a) are higher than in Fig. 13(b).

Fig. 14 presents the accumulated PSD values. Fig. 14(a) illustrates the PSD distributions within the thermal neutron peak window and the hydrogen peak window, while Fig. 14(b) shows the PSD distribution integrated over the entire energy range. In Fig. 14(a), within the thermal neutron peak window, PSD values near 0.6 (corresponding to gamma ray events) show negligible variation across different porosity conditions. In contrast, thermal neutron counts are noticeably higher than those under lowporosity conditions, aligning with theoretical predictions. In the hydrogen peak energy window, thermal neutrons do not contribute counts within this range, the PSD values around 0.7 accumulate to zero. In high-porosity formations with increased hydrogen content, the gamma ray counts corresponding to hydrogen are significantly higher than those in low-porosity reservoirs. Fig. 14(b) shows the PSD results accumulated over the entire energy range. Due to measurement errors in the pulse amplitude spectrum caused by low-energy particle incidence, the gamma peak on the left deviates from a Gaussian distribution and exhibits a broader spread. Conversely, the thermal neutron peak, characterized by a narrower energy distribution, follows a distinct Gaussian pattern. Furthermore, the differences in thermal neutron counts across porosity conditions are more pronounced than those observed for gamma rays, indicating that the equivalent gamma ray response of thermal neutrons exhibits higher sensitivity for porosity evaluation.

The Figure of Merit (FOM) is a standard metric in nuclear detector technology used to quantify the effectiveness of pulse shape discrimination method. A higher FOM value indicates better capability to distinguish between two particle types in the PSD spectrum. The FOM can be calculated using Eq. (13):

$$FOM = \frac{\Delta S}{\delta_n + \delta_{\gamma}} \tag{13}$$

where the ΔS is the distance from the center of the neutron peak to the center of the gamma peak, δ_n and δ_γ are the full widths at half maximum (FWHM) of the neutron and gamma peaks, respectively.

A larger FOM value reflects better separation of neutron and gamma ray peaks, enhancing the detector's capability to classify particle types accurately. The calculated FOM using the specified time window is 4.17, indicating that the 2D-PSD simulation results offer sufficient resolution for effective particle discrimination.

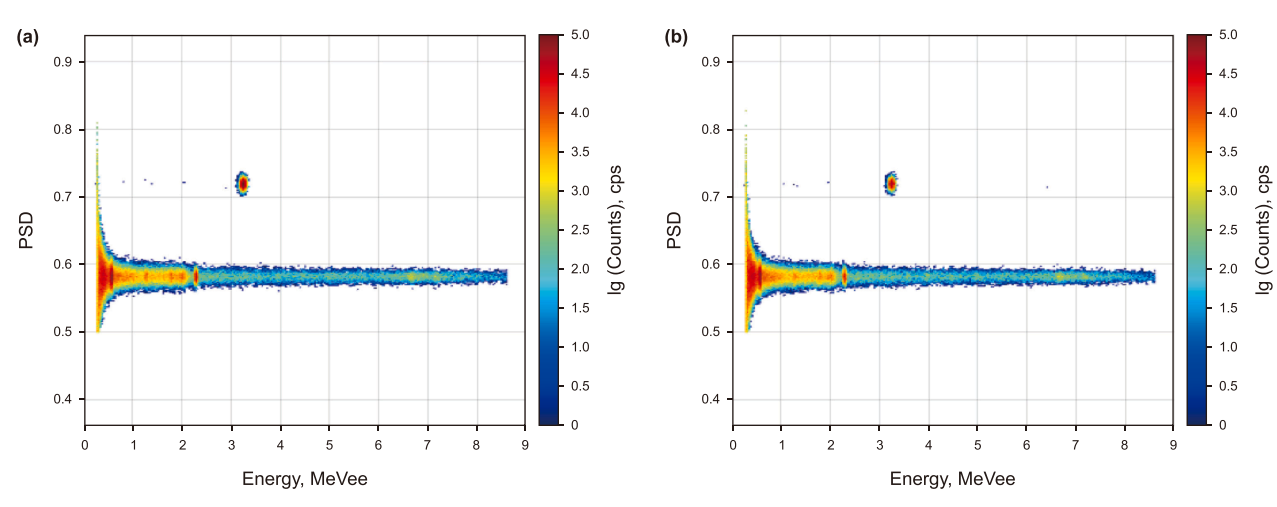
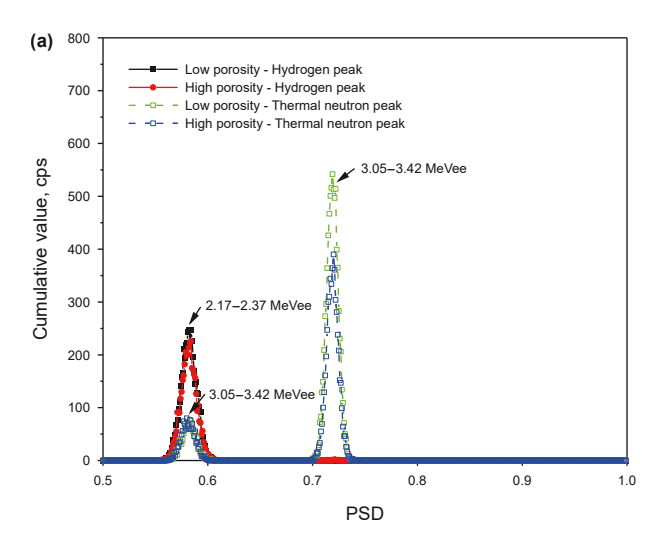


Fig. 13. 2D-PSD under different porosity conditions. (a) Low porosity water saturated formation. (b) High porosity water saturated formation.



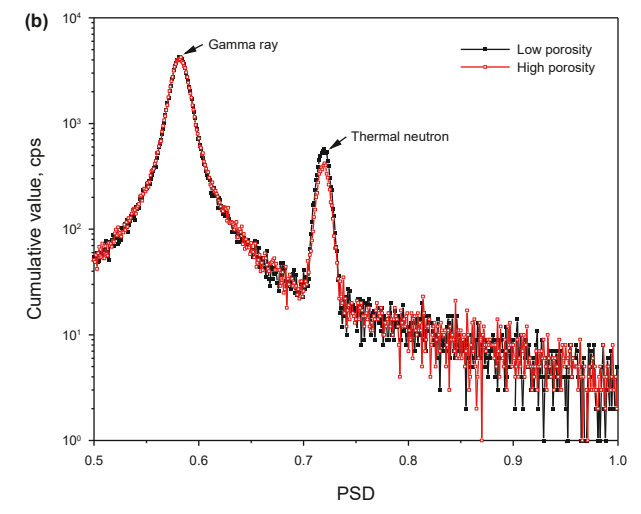


Fig. 14. Cumulative results of 2D-PSD in different energy windows. (a) Cumulative results in the energy window of thermal neutron or hydrogen element. (b) Cumulative results in the entire energy window.

(2) Logging response of equivalent gamma ray spectrum

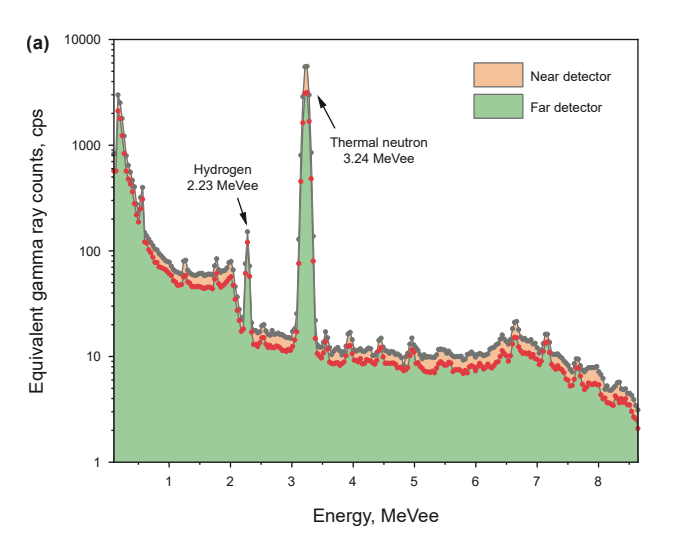
The energy spectrum, which reflects the response characteristic related to porosity and oil saturation, is obtained through FLUKA under various formation conditions. As shown in Fig. 15(a), a water saturated sandstone formation with 12% porosity is used to generate the logging response. The energy spectrum recorded by the far detector is represented by the red line, while the near detector is shown in black. Although the far detector has a longer spacing, as twice as the size of the near detector, resulting in lower counts. In the energy range of 3.24 MeVee, an obvious peak is observed in Fig. 15(a). This peak represents thermal neutrons caused by the luminescence of secondary charged particles, which are produced from the interaction of thermal neutrons with the CLYC materials.

Fig. 15(b) illustrates capture gamma ray spectrum of water saturated sandstone formation under different porosity conditions. As porosity increases, the hydrogen index rises, enhancing the slowing-down capability of the formation and resulting in a greater production of thermal neutrons near the D–T source.

However, due to diffusion effects, the number of thermal neutrons reaching the detector decreases. Besides, the number of capture gamma rays, which produced by capture interacting with formation nuclei in the formation, also decreases. According to the feature of equivalent capture gamma ray spectrum, the equivalent gamma ray with energy from 2.95 to 3.42 MeVee is used as the indicator of thermal neutron.

3.4.3. Porosity logging response of equivalent gamma ray counts ratios

Fig. 16 illustrates the responses of the dual-spacing thermal neutron count ratio and the equivalent gamma ray count ratio as functions of formation porosity. The thermal neutron count ratio is obtained using an instrument similar to that shown in Fig. 9(a), where the ratio of thermal neutron counts is recorded by ³Hetubes positioned at near and far spacings. Similarly, the equivalent gamma ray count ratio is derived from the same instrument depicted in Fig. 9(a), based on counts accumulated within the energy window of 2.95–3.42 MeVee in the equivalent gamma ray



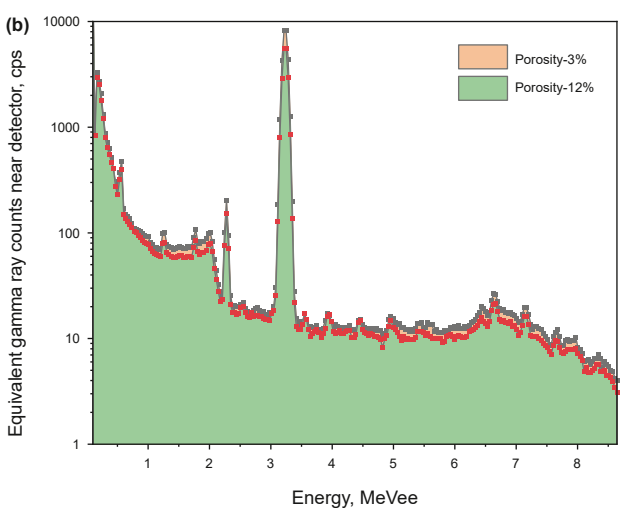


Fig. 15. Equivalent gamma ray spectrum recorded by CLYC detector. (a) Gamma ray spectrum recorded from near and far detector in capture gate. (b) Capture gamma ray spectrum recorded from near detector under different porosity.

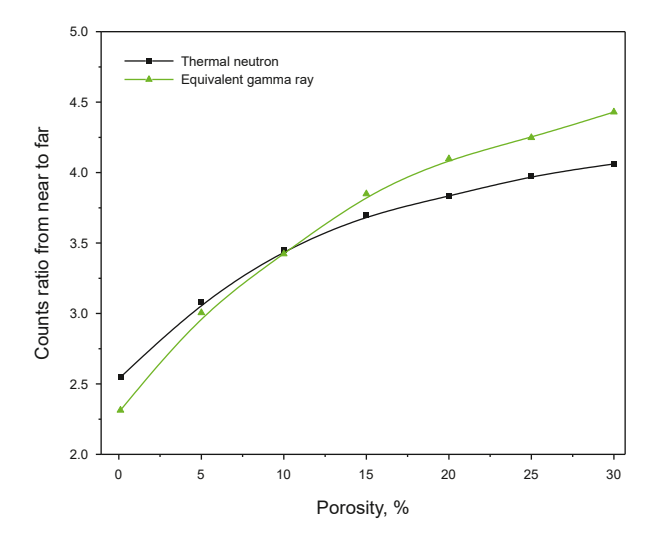


Fig. 16. Comparison of logging response for porosity evaluation.

spectrum. These gamma rays are recorded during the capture gate following a short-pulsed emission period.

As porosity increases, the response trends of the two count ratios remain generally consistent, although differences in sensitivity are evident. The thermal neutron counts ratio recorded by ³He-tubes is primarily determined by the slowing-down length of formation and reflects variations in the hydrogen index. The higher neutron energy enhances the contribution of inelastic scattering, resulting in reduced sensitivity of the D-T source ³He-based thermal neutron ratio in high-porosity formations. In contrast, the equivalent gamma ray counts from the spectrum includes gamma ray signals proportional to thermal neutron interactions, as well as a background component from capture gamma rays. The background is influenced by both the formation density and the neutron capture cross section. This multi-process sensitivity enhances the count ratio's responsiveness to porosity changes, thereby exhibiting a different behavior from the direct thermal neutron measurement of ³He-tubes. This consistency in response trend confirms that the CLYC-based equivalent gamma ray provides comparable porosity evaluation capability to conventional neutron porosity logging. These results validate the effectiveness and feasibility of the CLYC detector for application in neutron well

Conventional neutron porosity measurements are significantly influenced by formation lithology, necessitating the application of correction charts to obtain accurate water-filled porosity. Lithology is commonly identified using supplementary methods such as density logging, acoustic logging, and elemental spectroscopy logging, each of which may introduce additional sources of uncertainty into the porosity interpretation. The CLYC detector, through its ability to measure the equivalent gamma ray spectrum, enables the simultaneous extraction of both the ratio and elemental yields. This multi-parameter interpretation capability, which based solely on the detector's own response, reduces dependence on external measurements. As a result, the overall accuracy and reliability of porosity evaluation are substantially improved.

It should be noted that the actual downhole environment is considerably more complex than the idealized conditions employed in the simulation. Downhole conditions involve elevated ambient temperatures, intense mechanical vibrations, limited spatial availability, and a more intricate distribution of radiation sources—including scattered neutrons and capture

gamma rays originating from borehole components and surrounding formation materials. These factors can result in spectral broadening, variations in counting efficiency, and potential signal pile-up in high-flux regions. Therefore, although the simulation results confirm the feasibility and advantages of using CLYC detectors under controlled conditions, further experimental validation under downhole-simulated environments is essential to ensure reliable and robust detector performance in practical applications.

4. Conclusions

The excellent physical properties of the CLYC scintillator offer broad application prospects in the field of neutron and nuclear radiation detection. This study focused on evaluating the feasibility of applying CLYC detectors in nuclear well logging. The investigation was carried out from two main perspectives: numerical response simulation and practical well logging application. The main conclusions are as follows:

- (1) FLUKA-based Monte Carlo simulations method was conducted to model the interaction of thermal neutrons with the CLYC detector, and the results validated its response through agreement with experimental data. The Gamma ray spectra matched well in full-energy peak position, shape, and width, while neutron spectra effectively converted charged particle energy deposition into equivalent gamma ray peaks.
- (2) A pulse shape discrimination (PSD) simulation method based on probabilistic iteration was proposed, achieving accurate 2D-PSD modeling by accounting for energydependent attenuation effects.
- (3) The CLYC detector was integrated into a double-particle neutron well logging system, demonstrating consistent thermal neutron equivalent gamma count ratios with conventional ³He-tube-based methods. It also has ability to record gamma spectra enabled porosity, hydrocarbon saturation, and elemental yield evaluation.

With high detection efficiency, relatively good energy resolution, and a wide temperature range, the CLYC detector is well-suited for downhole neutron and gamma detection. This work established a foundation for advancing neutron-based double-particle logging technology.

CRediT authorship contribution statement

Qi-Xuan Liang: Writing – review & editing, Writing – original draft, Software, Methodology, Investigation, Data curation. **Feng Zhang:** Writing – review & editing, Supervision, Resources, Project administration, Methodology, Funding acquisition, Conceptualization. **Jun-Ting Fan:** Writing – review & editing, Validation, Formal analysis, Data curation. **Dong-Ming Liu:** Writing – review & editing, Funding acquisition, Formal analysis, Data curation. **Yun-Bo Zhou:** Writing – review & editing, Validation, Data curation. **Qing-Chuan Wang:** Writing – review & editing, Software. **Di Zhang:** Writing – review & editing, Investigation.

Declaration of competing interest

The authors declare the following financial interests/personal relationships which may be considered as potential competing interests: Feng Zhang reports financial support was provided by National Natural Science Foundation of China. If there are other authors, they declare that they have no known competing financial

interests or personal relationships that could have appeared to influence the work reported in this paper.

Acknowledge

The authors would like to acknowledge the support of the National Natural Science Foundation of China (42174147, 42474155), the Scientific and Technological Innovation Projects of Laoshan Laboratory (LSK|20220347).

References

- Battistoni, G., Boehlen, T., Cerutti, F., et al., 2015. Overview of the FLUKA code. Ann. Nucl. Energy 82, 10–18. https://doi.org/10.1016/j.anucene.2014.11.007.
- Beals, R., Hrametz, A., Jacobson, L.A., et al., 1993. Response characterization of an induced gamma spectrometry tool using A bismuth germanate scintillator. Log. Anal. 34. SPWLA-1993-v34n4a1. https://onepetro.org/petrophysics/article-abstract/170840/Response-Characterization-Of-An-Induced-Gamma.
- Bessiere, A., Dorenbos, P., Van Eijk, C.W.E., et al., 2004. New thermal neutron scintillators: Cs₂LiYCl₆: Ce³⁺ and Cs₂LiYBr₆: Ce³⁺. IEEE Trans. Nucl. Sci. 51, 2970–2972. https://doi.org/10.1109/TNS.2004.834957.
- Bessiere, A., Dorenbos, P., Van Eijk, C.W.E., et al., 2005. Luminescence and scintillation properties of Cs₂LiYCl₆: Ce³⁺ for γ and neutron detection. Nucl. Instrum. Methods Phys. Res. Sect. A Accel. Spectrom. Detect. Assoc. Equip. 537 (1–2), 242–246. https://doi.org/10.1016/j.nima.2004.08.018.
- Borella, A., Boogers, E., Rossa, R., et al., 2018. Characterization and Monte Carlo simulations for a CLYC detector. Int. J. Modern Phy. Con. Series. https://doi.org/ 10.1142/S2010194518601151.
- Budden, B.S., Stonehill, L.C., Dallmann, N., et al., 2015. A Cs₂LiYCl₆:Ce-based advanced radiation monitoring device. Nucl. Instrum. Methods Phys. Res. Sect. A Accel. Spectrom. Detect. Assoc. Equip. 784, 97–104. https://doi.org/10.1016/j.nima.2014.11.051.
- Chowdhury, P., Jackson, E.G., Lister, C.J., 2014. Fast neutron response of ⁶Li-depleted CLYC detectors up to 20 MeV. Nucl. Instrum. Methods Phys. Res. Sect. A Accel. Spectrom. Detect. Assoc. Equip. 763, 433–441. https://doi.org/10.1016/j.nima.2014.06.074.
- Combes, C.M., Dorenbos, P., Van Eijk, C.W.E., et al., 1999. Optical and scintillation properties of pure and Ce^{3+} -doped Cs_2LiyCl_6 and Li_3YCl_6 : Ce^{3+} crystals. J. Lumin. 82 (4), 299–305. https://doi.org/10.1016/S0022-2313(99)00047-2.
- D'olympia, N., Chowdhury, P., Lister, C.J., et al., 2013. Pulse-shape analysis of CLYC for thermal neutrons, fast neutrons, and gamma-rays. Nucl. Instrum. Methods Phys. Res. Sect. A Accel. Spectrom. Detect. Assoc. Equip. 714, 121–127. https://doi.org/10.1016/j.njma.2013.02.043
- Fan, J.L., Zhang, F., Tian, L.L., et al., 2021. A method of monitoring gas saturation in carbon dioxide injection heavy oil reservoirs by pulsed neutron logging technology. Petrol. Explor. Dev. 48 (6), 1420–1429. https://doi.org/10.1016/S1876-3804(21)60298-7.
- Glodo, J., Hawrami, R., Shah, K.S., 2013. Development of Cs₂LiYCl₆ scintillator. J. Cryst. Growth 379, 73–78. https://doi.org/10.1016/j.jcrysgro.2013.03.023.
- Guo, W.J., Goenawan, F., Mora, H., et al., 2024. Geochemistry and saturation applications utilizing a new slim pulsed neutron technology. In: 65th SPWLA Annual Logging Symposium. https://doi.org/10.30632/SPWLA-2024-0120.
- Hearst, J.R., Nelson, P.H., 1985. Well Logging for Physical Properties. Mc Graw-Hill Book Co, New York.
- Herron, S.L., Herron, M.M., 1996. Quantitative lithology: an application for open and cased hole spectroscopy. In: 37th SPWLA Annual Logging Symposium, SPWLA-1996-E. In: https://onepetro.org/SPWLAALS/proceedings-abstract/ SPWLA-1996/All-SPWLA-1996/19547.
- Hoyer, W.A., Rumble, R.C., 1965. Field experience in measuring oil content, lithology and porosity with a high-energy neutron-induced spectral logging system. J. Petrol. Technol. 17 (7), 801–807. https://doi.org/10.2118/988-PA.
- Jin, T.G., Hao, S.W., Shang, Y.F., et al., 2022. Recent trends in elpasolite single crystal scintillators for radiation detection. Crystals 12 (7), 887. https://doi.org/ 10.3390/cryst12070887.
- Kim, Y., Akang, N., 2024. Crucial factors for in-situ CO₂ monitoring in CO₂-EOR Projects using pulsed neutron well logging. In: SPE Gas & Oil Technology Showcase and Conference. https://doi.org/10.2118/219169-MS.
- Lee, D.W., Stonehill, L.C., Klimenko, A., et al., 2012. Pulse-shape analysis of Cs₂LiYCl₆:Ce scintillator for neutron and gamma-ray discrimination. Nucl. Instrum. Methods Phys. Res. Sect. A Accel. Spectrom. Detect. Assoc. Equip. 664 (1), 1–5. https://doi.org/10.1016/j.nima.2011.10.013.
- Lewis, E.E., Miller, W.F., 1984. Computational Methods of Neutron Transport. John Wiley and Sons, Inc., New York.
- Machicote, S., De Lisio, S., Pirrone, M., 2023. The effective diagnostic capability of pulsed neutron well logging for CCS monitoring purposes. In: 64th SPWLA Annual Logging Symposium. https://doi.org/10.30632/SPWLA-2023-0055.
- Machrafi, R., Miller, A.L., Khan, N., 2015. New approach to neutron spectrometry with multi element scintillator. Radiat. Meas. 80, 10–16. https://doi.org/ 10.1016/j.radmeas.2015.06.009.

- Machrafi, R., Khan, N., Miller, A.L., 2014. Response functions of Cs₂LiYCl₆: Ce scintillator to neutron and gamma radiation. Radiat. Meas. 70, 5–10. https://doi.org/10.1016/j.radmeas.2014.07.010.
- Odom, R., Albert, L., Camacho, J., et al., 2013. Application of a new multi-detector pulsed-neutron system in a CO₂ flood of a mature field. In: 54th SPWLA Annual Logging Symposium, SPWLA-2013-XXX. In: https://onepetro.org/SPWLAALS/proceedings-abstract/SPWLA13/All-SPWLA13/28335.
- Odom, R., Dahlin, T., Dolliver, D., et al., 2008. Design and initial field-test results of a new pulsed neutron well logging system for cased reservoir characterization. In: 49th SPWLA Annual Logging Symposium, SPWLA-2008-O. In: https://onepetro.org/SPWLAALS/proceedings-abstract/SPWLA08/All-SPWLA08/27868.
- Pérez-Loureiro, D., Kamaev, O., Bentoumi, G., et al., 2021. Evaluation of CLYC-6 and CLYC-7 scintillators for detection of nuclear materials. Nucl. Instrum. Methods Phys. Res. Sect. A Accel. Spectrom. Detect. Assoc. Equip. 1012, 165622. https://doi.org/10.1016/j.nima.2021.165622.
- Pontecorvo, B., 1941. Neutron well logging-a new geological method based on nuclear physics. Oil Gas J. 40, 18.
- Qin, J.G., Lai, C.F., Lu, X.X., et al., 2018. Characterization of a 6Li enriched Cs₂LiYCl₆: Ce scintillator and its application as a γ-ray detector. Nucl. Instrum. Methods Phys. Res. Sect. A Accel. Spectrom. Detect. Assoc. Equip. 886, 55–60. https://doi.org/10.1016/j.nima.2017.11.053.
- Rider, M.H., 1986. The Geological Interpretation of Well Logs. John Wiley and Sons, Inc., New York.
- Rose, D., Zhou, T., Beekman, S., et al., 2015. An innovative slim pulsed neutron well logging tool. In: 56th SPWLA Annual Logging Symposium. SPWLA-2015-XXXX. https://onepetro.org/SPWLAALS/proceedings-abstract/SPWLA15/All-SPWLA15/28523.
- Schneider, D.M., Hubner, B.G., 1991. Neutron/gamma discrimination in a lithium-6 glass scintillator in an MWD tool. In: Conference Record of the 1991. IEEE Nuclear Science Symposium and Medical Imaging Conference. https://doi.org/10.1109/NSSMIC.1991.259096.
- Schultz, W.E., Smith Jr, H.D., 1974. Laboratory and field evaluation of a carbon/oxygen (C/O) well logging system. J. Petrol. Technol. 26 (10), 1103–1110. https://doi.org/10.2118/4638-PA.
- Scott, H.D., Stoner, C., Roscoe, B.A., et al., 1991. A new compensated through-tubing carbon/oxygen tool for use in flowing wells. In: 32nd SPWLA Annual Logging Symposium. SPWLA-1991-MM. https://onepetro.org/SPWLAALS/proceedingsabstract/SPWLA-1991/All-SPWLA-1991/18923.
- Smith, M.B., McClish, M., Achtzehn, T., et al., 2013. Assessment of photon detectors for a handheld gamma-ray and neutron spectrometer using Cs₂LiYCl₆:Ce (CLYC) scintillator. Nucl. Instrum. Methods Phys. Res. Sect. A Accel. Spectrom. Detect. Assoc. Equip. 715, 92–97. https://doi.org/10.1016/j.nima.2013.03.023.
- Tittle, C.W., Faul, H., Goodman, H., 1951. Neutron well logging of drill holes: the neutron-neutron method. Geophysics 16 (4), 626–658. https://doi.org/10.1190/
- Tittle, C.W., 1961. Theory of neutron logging I. Geophysics 26 (1), 27–39. https://doi.org/10.1190/1.1438839.
- Tittman, J., Nelligan, W.B., 1960. Laboratory studies of a pulsed neutron-source technique in well logging. J. Petrol. Technol. 12 (7), 63–66. https://doi.org/10.2118/1227-G.
- Tsorbatzoglou, K., McKeag, R.D., 2011. Novel and efficient 10B lined tubelet detector as a replacement for 3He neutron proportional counters. Nucl. Instrum. Methods Phys. Res. Sect. A Accel. Spectrom. Detect. Assoc. Equip. 652 (1), 381–383. https://doi.org/10.1016/j.nima.2010.08.102.
- Van Loef, E.V.D., Dorenbos, P., Van Eijk, C.W.E., et al., 2002. Scintillation and spectroscopy of the pure and Ce³⁺-doped elpasolites: Cs₂LiYX₆ (X= Cl, Br). J. Phys. Condens. Matter 14 (36), 8481. https://doi.org/10.1088/0953-8984/14/
- Van Loef, E.V.D., Glodo, J., Higgins, W.M., et al., 2005. Optical and scintillation properties of Cs₂LiYCl₆:Cc³⁺ and Cs₂LiYCl₆:Pr³⁺ crystals. IEEE Trans. Nucl. Sci. 52 (5), 1819–1822. https://doi.org/10.1109/TNS.2005.856812.
- Wang, H., Yue, A.Z., Zhang, X.L., et al., 2022. Bulk density response and experimental study of pulsed neutron-gamma density logging. Front. Earth Sci. 10, 803775. https://doi.org/10.3389/feart.2022.803775.
- Wang, H., Yue, A.Z., Wang, S.S., et al., 2020. On density sensitivity of pulsed neutron-gamma density logging tools. Well Logging Technol. 44 (2), 159–164. https://doi.org/10.16489/j.issn.1004-1338.2020.02.009 (in Chinese).
- Wen, X.F., Enqvist, A., 2017. Measuring the scintillation decay time for different energy deposited by γ-rays and neutrons in a Cs₂LiYCl₆: Ce³⁺ detector. Nucl. Instrum. Methods Phys. Res. Sect. A Accel. Spectrom. Detect. Assoc. Equip. 853, 9–15. https://doi.org/10.1016/j.nima.2017.02.019.
- Yang, K., Menge, P.R., 2015. Pulse shape discrimination of Cs₂LiYCl₆:Ce³⁺ scintillator from –30 °C to 180 °C. Nucl. Instrum. Methods Phys. Res. Sect. A Accel. Spectrom. Detect. Assoc. Equip. 784, 74–79. https://doi.org/10.1016/j.nima.2014.08.031.
- Youmans, A.H., Hopkinson, E.C., Bergan, R.A., et al., 1964. Neutron lifetime, a new nuclear log. J. Petrol. Technol. 16 (3), 319–328. https://doi.org/10.2118/709-PA.
- Zhao, K., Huang, Y., Shan, C., et al., 2023. A low-power neutron and gamma-ray detector for environmental radiation monitoring using CLYC scintillator. J. Instrum. 18 (9), P09043. https://doi.org/10.1088/1748-0221/18/09/P09043.